

Wicking flow through microchannels

Hadi Mehrabian,¹ Peng Gao,² and James J. Feng^{1,3,a)}

¹*Department of Chemical and Biological Engineering, University of British Columbia, Vancouver, British Columbia V6T 1Z3, Canada*

²*Department of Modern Mechanics, University of Science and Technology of China, Hefei, Anhui 230026, China*

³*Department of Mathematics, University of British Columbia, Vancouver, British Columbia V6T 1Z2, Canada*

(Received 12 July 2011; accepted 2 December 2011; published online 27 December 2011)

We report numerical simulations of wicking through micropores of two types of geometries, axisymmetric tubes with contractions and expansions of the cross section, and two-dimensional planar channels with a Y-shaped bifurcation. The aim is to gain a detailed understanding of the interfacial dynamics in these geometries, with an emphasis on the motion of the three-phase contact line. We adopt a diffuse-interface formalism and use Cahn-Hilliard diffusion to model the moving contact line. The Stokes and Cahn-Hilliard equations are solved by finite elements with adaptive meshing. The results show that the liquid meniscus undergoes complex deformation during its passage through contraction and expansion. Pinning of the interface at protruding corners limits the angle of expansion into which wicking is allowed. For sufficiently strong contractions, the interface negotiates the concave corners, thanks to its diffusive nature. Capillary competition between branches downstream of a Y-shaped bifurcation may result in arrest of wicking in the wider branch. Spatial variation of wettability in one branch may lead to flow reversal in the other. © 2011 American Institute of Physics. [doi:10.1063/1.3671739]

I. INTRODUCTION

Wicking is the suction of a liquid by the negative capillary pressure due to the meniscus curvature. It is a key mechanism for two-phase flow in porous media.¹ To model such flows, an extended Darcy's law is often used to relate the pressure drop to the flow rate, with an empirical *relative permeability* expressed in terms of the local saturation via the Leverett J-function.² The drawback of such an approach is its empirical nature; the actual pore geometry and interfacial morphology, which play important roles in two-phase flow through porous medium, are not explicitly accounted for. Recently, wicking has figured prominently in water transport in the gas diffusion medium of proton-exchange-membrane fuel cells,³ and in microfluidics for chemical analysis and biological assay.^{4,5} These typically involve wicking in one or multiple flow conduits of complex geometry. To a large degree, the interfacial morphology and motion determine the efficacy and efficiency of the devices.

There are theoretical and numerical difficulties in computing wicking flows through complex geometries. These include the lack of a good model for the moving contact line, the need to capture dynamically a moving and deforming interface, morphological singularities in coalescence and rupture of interfaces, and the complex flow geometries in practically interesting problems. The first three are generic to simulation of interfacial flows. The last, on geometry, is especially pertinent to flow in porous medium. The geometric features of a pore include changes in the cross-sectional area between wide pore chambers and narrow pore throats, branching and inter-

section of pores, and the appearance of sharp edges and corners on which a gas-liquid interface can be pinned.

The classic work on wicking flows is that of Lucas⁶ and Washburn,⁷ who computed capillary rise in straight tubes. This solution is notable for its simplicity. Dynamics of the meniscus is completely ignored. In its place, a static interfacial shape is assumed such that the interface merely supplies a constant suction pressure. In addition, the flow in the tube is taken to be fully developed Poiseuille flow. Now the capillary rise can be computed by balancing the capillary pressure against the viscous friction. Later work has sought to include inertia, dynamic contact angle and entry effects.⁸⁻¹² More recently, tubes of non-circular cross sections have also been considered.¹³

Of more relevance to our work are generalizations of the Lucas-Washburn solution to tubes and channels of gradually varying cross sections. Using the lubrication approximation, *one-dimensional* (1D) solutions have been obtained for sinusoidal tubes,^{14,15} sinusoidal tubes with tortuosity¹⁶ and tubes and channels with convergent, divergent, and power-law cross sections.¹⁷ Liou *et al.*¹⁸ extended the previous solutions to 2D axisymmetric flows by using approximate velocity profiles. This allowed them to include inertia as well as viscous stresses that vary with the cross-sectional area. However, a common feature of all these studies is that they ignore dynamics at the meniscus. The capillary pressure is quasi-statically equilibrated along the meniscus, thus giving it a spherical shape, whose curvature is used to compute the capillary pressure via the Young-Laplace equation. The main finding is a geometric effect on the meniscus movement: wicking goes faster in convergent than divergent channels. In the former, the meniscus curvature and hence the capillary suction increase downstream.

^{a)} Author to whom correspondence should be addressed. Electronic mail: jfeng@chbe.ubc.ca.

The only numerical study of wicking flow inside tubes with convergent-divergent cross section is done by Erickson *et al.*¹⁹ They have computed the 2D axisymmetric flow inside tubes by finite elements, but excluded the hydrodynamics of the interface as in the analytical studies mentioned above. By assuming a spherical shape of the meniscus, they update its position from the liquid volume flow rate. The capillary pressure is introduced by the Young-Laplace equation along with a dynamic contact angle. Perhaps to minimize the disturbance to the meniscus and to make the spherical shape a more accurate approximation, they have used very long tubes with exceedingly mild contractions and expansions, with a contraction/expansion angle of 0.5° . A surprising prediction is that if the total lengths of the wider and narrower portions of the tube are fixed, the time for the meniscus to pass through the tube is independent of the number of the contraction/expansion cycles along the tube's length.

To summarize this brief review of the literature, previous studies have ignored the hydrodynamics of the meniscus. The motion of the contact line is unaccounted for, and the meniscus shape is always prescribed to be spherical. Little can be found in the literature that deals with the detailed morphological changes of the meniscus during its motion through complex geometries. As such, their applicability to two-phase transport in porous media is quite limited. For one, pinning of the interfaces on sharp corners of the pore is responsible for pore blockage and, if external pressure is applied, eventual capillary breakthrough.^{20,21} Competition among interconnected pores is considered the key mechanism in developing a tree-like morphology of water transport in the gas diffusion medium (GDM) of fuel cells.^{3,22} Such competition will depend on the dynamics of the interfaces in complex geometries, including rupture and coalescence as the meniscus negotiates bifurcations and junctions. Finally, the wettability of porous medium is often manipulated to enhance two-phase transport.²³ The underlying mechanism has to be sought from the hydrodynamics of the interface. In this context, a fundamental understanding of interfacial dynamics during wicking through complex geometry is essential. In view of the various difficulties mentioned above, however, a rigorous study of the dynamics of the meniscus based on hydrodynamic principles has yet to be done.

This paper presents an initial effort toward addressing these issues. Physically, we will use the Cahn-Hillard diffuse-interface model to describe the contact line dynamics.²⁴ The contact line singularity is regularized by diffusion between the two phases. This allows us to integrate the microscopic physics into the macroscopic flow, and to capture the moving interface and its morphological changes accurately and naturally, including pinning at sharp corners and otherwise singular interfacial breakup at bifurcations. Geometrically, we examine the two quintessential features of a porous medium: the areal changes between pore throats and chambers and the branching of flow conduits. Specifically, we simulate the wicking flow in axisymmetric tubes with non-uniform cross sections and 2D planar channels that bifurcate into two branches. We show that the meniscus undergoes complex deformations through contractions and expansions, with contact line pinning at protruding corners and turning of the

interface at concave corners. The assumption of a spherical interface is appropriate only in special cases, e.g., in straight and expanding tubes, where the dynamics is sufficiently slow to allow equilibration of the capillary pressure along the meniscus. Capillary competition between bifurcating channels may suppress wicking in the wider branch in favor of the narrower one. Manipulating the wettability in the branches can even produce flow reversal.

II. DIFFUSE-INTERFACE MODEL AND PROBLEM SETUP

We adopt a diffuse-interface model in which the two fluid components, say, air and water, are viewed as mixing to a limited extent in a narrow interfacial layer. A scalar *phase field* ϕ is introduced to distinguish the components such that $\phi = 1$ in the liquid, $\phi = -1$ in the gas, and $\phi = 0$ gives the position of the interface. Interfacial mixing is governed by a mixing energy²⁵

$$f_{mix}(\phi, \nabla\phi) = \frac{\lambda|\nabla\phi|^2}{2} + \frac{\lambda}{4\epsilon^2}(\phi^2 - 1)^2, \quad (1)$$

where λ is the mixing energy density and ϵ is the interfacial thickness. In the limit of thin interfaces, the classical concept of interfacial tension σ can be recovered from the mixing energy

$$\sigma = \frac{2\sqrt{2}\lambda}{3\epsilon}. \quad (2)$$

The evolution of ϕ is governed by the Cahn-Hillard equation²⁵

$$\frac{d\phi}{dt} = \nabla \cdot (\gamma \nabla G), \quad (3)$$

where γ is the mobility parameter and assumed to be constant, and the chemical potential

$$G = -\lambda \nabla^2 \phi + \frac{\lambda}{\epsilon^2} \phi(\phi^2 - 1) \quad (4)$$

is the variation of the mixing energy with respect to ϕ .

Wicking is significant in small capillary tubes and pores, and the resulting Reynolds and Bond numbers are typically much below unity. Therefore, we will neglect inertia and gravity throughout this work, and highlight the roles of capillarity and viscosity. The hydrodynamics is governed by the continuity equation and a modified Stokes equation

$$\nabla \cdot \mathbf{v} = 0, \quad (5)$$

$$G \nabla \phi + \nabla \cdot (\mu \nabla \mathbf{v}) - \nabla p = 0, \quad (6)$$

where \mathbf{v} is the velocity and p is the pressure. The term $G \nabla \phi$ represents the role of interfacial tension in the momentum equation.^{26,27} In the diffuse-interface framework, the interface is no longer treated as a boundary and these equations apply to the flow of both components. In the interfacial region, \mathbf{v} may be viewed as a volume-averaged velocity and

μ as an average viscosity. Equations (3), (5), and (6) are the governing equations of the problem. With convection, the left hand side of Eq. (3) is viewed as the material derivative: $d\phi/dt = \partial\phi/\partial t + \mathbf{v} \cdot \nabla\phi$.

The computational domain is illustrated in Fig. 1. Natural boundary conditions are employed at the inlet and the outlet. In addition, the pressure is set to be equal between the inlet and the outlet such that the motion of the liquid column is driven entirely by wicking, i.e., by the capillary pressure generated by the meniscus. On the solid walls, the following boundary conditions are imposed:

$$\mathbf{v} = 0, \quad (7)$$

$$\mathbf{n} \cdot \nabla G = 0, \quad (8)$$

$$\lambda \mathbf{n} \cdot \nabla \phi + f'_w(\phi) = 0, \quad (9)$$

where the normal vector \mathbf{n} points into the solid wall. Equation (7) is the no-slip condition on the wall, and Eq. (8) dictates zero flux through it. Equation (9) is the natural boundary condition arising from the variation of the wall energy f_w

$$f_w = -\sigma \cos \theta \frac{\phi(3 - \phi^2)}{4} + \frac{\sigma_{w1} + \sigma_{w2}}{2}, \quad (10)$$

which is the interaction energy between the fluid components and the solid substrate.²⁴ At $\phi = \pm 1$, i.e., away from the contact line, f_w should give the fluid-wall interfacial tension for the two fluids, σ_{w1} and σ_{w2} . This requirement leads to Young's equation that prescribes the static contact angle θ

$$\cos \theta = \frac{\sigma_{w2} - \sigma_{w1}}{\sigma}. \quad (11)$$

It may be shown that to leading order, Eq. (9) constrains the dynamic contact angle to be equal to the static one.^{24,28} For simplicity, we disregard contact angle hysteresis.

We solve the governing equations using a finite-element package AMPHI in axisymmetric or planar 2D geometries. Yue *et al.*²⁷ and Zhou *et al.*²⁹ have described the numerical algorithm in detail, presented numerical experiments on grid and time-step refinements and validated the methodology against numerical benchmarks. The numerical package has been applied to a number of interfacial-

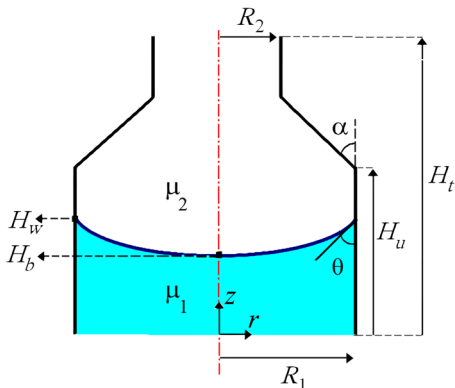


FIG. 1. (Color online) Schematic of the flow geometry for wicking into a capillary tube with contraction.

dynamics simulations.^{30–34} Here, we will only note a few important features. The equations are discretized using finite elements on an unstructured grid. The diffuse interface is resolved using adaptive meshing,³⁵ with the grid being dynamically refined and coarsened, respectively, upstream and downstream of the moving interface. The interfacial thickness ϵ is such that the sharp-interface limit is reached and the numerical results no longer depend on it.^{29,32} Besides, the grid is sufficiently refined to ensure convergence with decreasing grid size; the finest grid at the interface is on the order of $\epsilon/2$. Time-stepping is done in a second-order implicit scheme, with the nonlinear algebraic equations being solved by Newton iteration at each step.

The wicking flow consists in a column of hydrophilic fluid of viscosity μ_1 displacing a hydrophobic one of viscosity μ_2 (Fig. 1). The geometrical parameters include the contraction or expansion angle α , the total length H_t , length of the upstream section H_u , and the larger and smaller tube radii R_1 and R_2 . In Fig. 1, H_b denotes the position of the center of the meniscus, hereafter called its *base point*. H_w marks the position of the contact line on the wall, hereafter called the *wall point* of the meniscus. Initially, there is no flow and the liquid column is at $H_w = H_0$. Later, both H_w and H_b vary in time as the wicking proceeds. In this dynamic process, the interface shape is determined by the viscous and capillary forces and is in general not spherical. However, it will prove convenient to use an *effective curvature* κ , defined for a spherical surface, in discussing the evolution of the interface. From the height of the meniscus $\delta = H_w - H_b$ and the local tube radius R , we can calculate the radius of the spherical surface that passes through the wall and base points of the meniscus: $\rho = \frac{R^2 + \delta^2}{2\delta}$, from which we can define

$$\kappa = \frac{2\delta}{R^2 + \delta^2}. \quad (12)$$

Note that κ is an overall indication of the meniscus curvature and does not reflect the local deformation of the interface. It varies along the axis in an expansion or contraction as R does. In presenting results in dimensionless form, we scale length by R_1 , curvature by R_1^{-1} , velocity by σ/μ_1 and time by $\mu_1 R_1/\sigma$. Throughout this paper, we have set $R_2/R_1 = 0.5$ and $H_u/R_1 = 20$ except in Fig. 10 where $H_u/R_1 = 21$.

The physical parameters of the problem can be combined into two dimensionless parameters: the static contact angle θ and the viscosity ratio $m = \mu_2/\mu_1$. Unless noted otherwise, m is set to 0.02 to represent the viscosity ratio between air and water at room temperature. In addition, the diffuse-interface model introduces two additional lengths:³² the interfacial thickness ϵ and a *diffusion length* $l_d = \gamma^{1/2}(\mu_1\mu_2)^{1/4}$. They produce two more dimensionless parameters: the Cahn number $Cn = \epsilon/R_1$ and $S = l_d/R_1$. The choice of their values is fundamental to diffuse-interface computations and will be discussed next.

III. SHARP-INTERFACE LIMIT AND DIFFUSION LENGTH

The Cahn-Hilliard model formulated above has two parameters that have no counterparts in conventional Navier-

Stokes problems: the interfacial thickness ϵ and the diffusion length l_d . As explained by Yue *et al.*,³² ϵ or the Cahn number Cn should be sufficiently small so that the numerical results no longer depend on it; this is known as the sharp interfacial limit. The diffusion length l_d or the parameter S , on the other hand, should be chosen to match a single experimental measurement. In this section, we examine these issues in the simple geometry of imbibition and drainage in a straight capillary tube. Our aim is threefold: to ensure that the sharp-interface limit for moving contact lines is achieved, to select a suitable value for S , and to validate the numerical results for a straight circular tube against the Lucas-Washburn formula.^{6,7}

A. Sharp-interface limit

Real interfaces, a few nanometers in thickness, are typically not resolvable in macroscopic flow simulation. Thus, the diffuse-interface method uses an artificial ϵ that may be much larger than the real value. This is allowable if the sharp-interface limit is achieved, when ϵ and Cn are sufficiently small, such that the results are not affected by the unrealistic thickness of the interface.^{32,36} For interfacial flows without contact lines, the sharp-interface limit is typically approached at $Cn \sim 0.01$.²⁷

With moving contact lines, Yue *et al.*³² have shown that the achievement of sharp-interface limit is also dependent on the diffusion length. For Couette and Poiseuille flows with a transverse interface, they found that the location of the meniscus converges to a unique solution after Cn falls below a threshold $Cn \approx 4S$ and suggested this as the criterion for achieving the sharp-interface limit. In our wicking problem, the criterion turns out to be more stringent than that of Yue *et al.*³² We tested a range of Cn values for $S=0.04$, and found the results to be essentially independent of Cn once it is below 0.02. Figure 2 shows that the contact line motion and the meniscus shape agree closely between $Cn=0.02$ and $Cn=0.01$. Thus, the sharp-interface limit is achieved by using $Cn=0.02$ in this case.

B. Diffusion length

In simulating suspended drops and bubbles, the Cahn-Hilliard diffusion across the interface, represented by l_d or S , is immaterial as long as the sharp-interface limit is achieved.^{37,38} If an interface intersects a solid substrate, on the

other hand, the motion of the contact line is affected by this interfacial diffusion. Thus, l_d has the more physical meaning of the slip length, and its value must be chosen judiciously, e.g., to coincide with an experimental measurement.³²

In the capillary rise problem, the Lucas-Washburn formula^{6,7}

$$H(t) = \sqrt{H_0^2 + \frac{\sigma R \cos \theta (t - t_0)}{2\mu}} \quad (13)$$

is widely accepted as an accurate representation of the interfacial movement, as long as the liquid column is long enough such that the “end effect” is negligible and the flow can be approximated by the Poiseuille flow. Here, R is the tube radius, μ is the viscosity of the liquid and that of the gas is neglected.

Figure 3 compares our diffuse-interface calculation of capillary imbibition and drainage at several S values with the Lucas-Washburn formula. A few observations can be made. First, in both imbibition and drainage, the numerical result approaches the analytical formula as S increases. While the analytical solution neglects the dynamics at the meniscus and the contact line completely, the Cahn-Hilliard model includes a friction at the contact line in terms of an additional dissipation.²⁷ As the diffusion length or S increases, the effective slippage at the contact line increases, thus reducing the influence of this friction. For $S=0.04$, the effective curvature of the interface is 5% lower than that expected of a spherical surface. This is due to the flow effects at the meniscus that the Lucas-Washburn formula disregards.

Second, the contact line speed is insensitive to S . With a tenfold change in S , the contact line speed changes by some 6%. This forms an interesting contrast to the situation studied by Yue *et al.*,³² where in shear flows the meniscus shape or interface inclination is highly sensitive to S . This can be rationalized by the fact that the contact line speed is determined by equating the viscous dissipation to the surface energy gained by wetting or dewetting. Thus, insofar as most of the dissipation occurs in the bulk of the column, the effect of S is mild. In shear flows, in contrast, the contact line speed is prescribed, and the amount of Cahn-Hilliard diffusion affects the shape of the interface greatly.

Third, the same S produces larger deviation from the Lucas-Washburn formula for imbibition than for drainage.

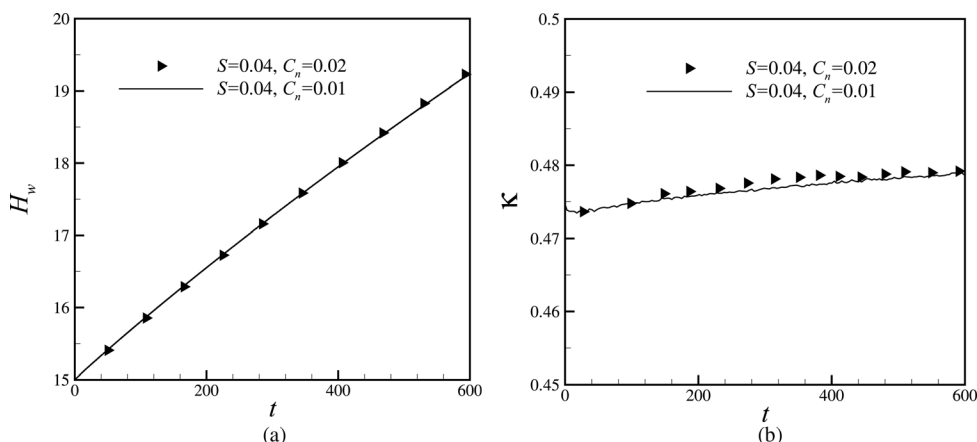


FIG. 2. Sharp-interface limit for computing capillary rise. (a) Contact line motion indicated by the rise of H_w in time for two Cahn numbers $Cn = 0.01$ and 0.02 . (b) Variation of the effective meniscus curvature κ with time for the same two Cn values. $S = 0.04$, $\theta = 60^\circ$, the tube radius $R = 1$, total length $H_l = 20$ and the initial column height $H_0 = 15$.

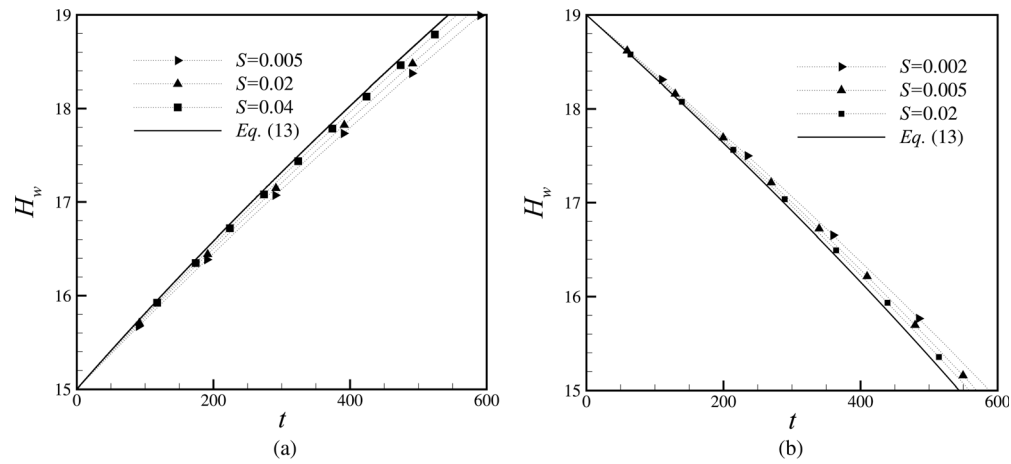


FIG. 3. Comparison between diffuse-interface simulation and the analytical Lucas-Washburn formula at different S values. (a) Imbibition with $\theta = 60^\circ$, $Cn = 0.01$, $m = 0.02$, and $H_0 = 15$. (b) Drainage with $\theta = 120^\circ$, $Cn = 0.01$, and $H_0 = 19$. Now, the less viscous component is wetting, and the non-wetting-to-wetting viscosity ratio $m = 50$.

This reflects the fact that the viscosity of the displacing and the displaced components contributes to the contact line motion differently. But this asymmetry is not reflected by the definition of S used here. Finally, there is an upper limit to reasonable S values. Using too large, a diffusion length l_d exaggerates the area that is directly affected by the contact line. Our numerical experiment shows that for $S = 0.15$, for example, the overall features of the flow are distorted by the interfacial diffusion, and the solution becomes very inaccurate. In typical flow situations, the slip length is orders of magnitude smaller than the macroscopic length scale.^{28,39}

To sum up this section, we have demonstrated how the sharp-interface limit can be achieved by using a small enough Cn and how S can be selected by comparing with the Lucas-Washburn formula. Most of the results to be presented are for $S = 0.04$ and $Cn = 0.01$. For the wicking through multiple contraction-expansion combinations (Fig. 10), we have used $Cn = 0.02$. To better resolve contact line pinning and turning at corners (e.g., Figs. 4 and 7), we have used a smaller $Cn = 0.005$.

IV. WICKING IN A TUBE WITH CONTRACTION OR EXPANSION

We consider the wicking flow of a liquid column into an axisymmetric tube, with a contraction as shown in Fig. 1 or with an expansion. The goal is to elucidate the detailed hydrodynamics of the moving interface, in particular, how the contact line negotiates concave and convex corners. Also of interest is the passage time as a function of the flow geometry, with a single contraction-expansion combination or multiple cycles of it.

A. Contraction

Figure 4 illustrates the wicking of a liquid through a 2:1 contraction at contraction angle $\alpha = 45^\circ$. The wall is hydrophilic to the liquid, with a wetting angle $\theta = 60^\circ$. The evolution of the interface is punctuated by several critical points marked on the $H_b \sim H_w$ and $\kappa \sim H_w$ curves as well as by the insets. In the first stage of the process ($H_w < H_u$), the meniscus moves with a constant shape within the wide tube before

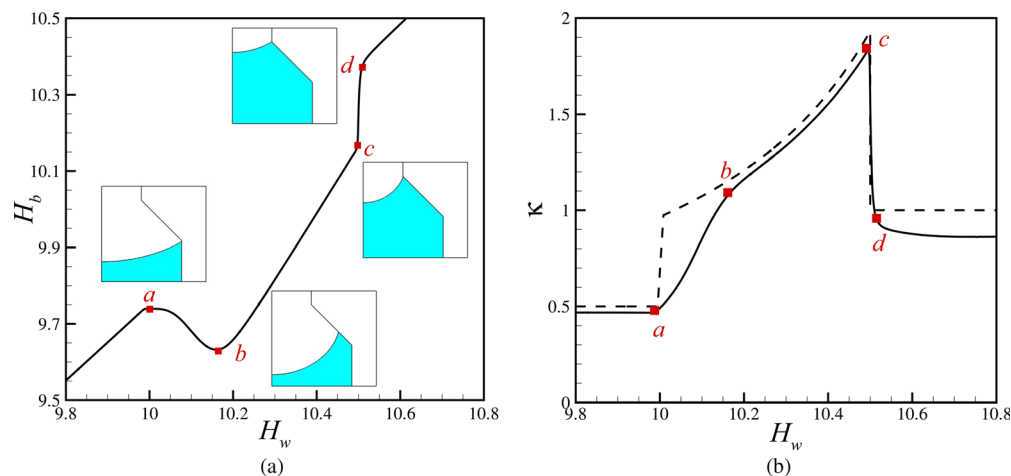


FIG. 4. (Color online) Meniscus movement through a contraction with $\alpha = 45^\circ$ represented by: (a) the variation of the base point with the wall point, and (b) the effective curvature defined in Eq. (12). $\theta = 60^\circ$, $Cn = 0.005$, and $H_u = 10$. In (a) the insets correspond to the four points marked by squares on the curve. In (b) the dashed line indicates the curvature expected of a quasi-static spherical meniscus.

it reaches the contraction. The base point and wall point advance at equal speed and the trajectory in Fig. 4(a) is a straight line with slope 1. The meniscus is not spherical, however. Viscous forces distort it so that the constant effective curvature κ is 6% below that expected of a spherical meniscus at equilibrium in the upstream portion of the tube.

As the contact line reaches the corner at the beginning of the contraction, marked by point a in the plot, a new behavior sets in. First, the contact line quickly moves past the concave corner. Once it is on the inclined wall of the contraction, the interface must rotate by α to maintain the same contact angle θ with the wall. This rotation first occurs locally at the contact line, elevating the local curvature. Then, the interfacial distortion propagates toward the center by interfacial tension, causing the central portion of the meniscus to pull back upstream. This process is reflected in Fig. 4(a) by the downturn of the trajectory and the sharp upturn of κ in Fig. 4(b). The interfacial adjustment is completed by point b , when the base point of the interface is at a minimum. During this highly dynamic transition, κ falls far below what one would expect by assuming a quasi-static spherical meniscus.

After point b , the base point moves forward again, and at a higher speed than the wall point because R is shrinking, and the interface is continuously becoming more curved. Hence, the continued increase in κ . The next milestone is when the contact line reaches the convex corner marking the end of the contraction (point c). The contact line is *pinned* at the corner,⁴⁰ while the base point continues to move forward. Thus, the interface rotates toward the downstream as if hinged at the corner, and in the mean time straightens with a steep decline in κ . The pinning ends when the angle between the interface and an extension of the downstream wall reaches the contact angle θ , in accordance with Gibbs' pinning criterion, and the meniscus as a whole moves into the narrow channel. This moment is marked by d in Fig. 4. The effective curvature κ settles into a steady value roughly 14% below that for a perfectly spherical meniscus at equilibrium.

B. Regularization of corner singularity

The turning of the interface at the concave corner (point a) deserves a closer examination. The case illustrated in Fig. 4 has a relatively mild contraction with $\alpha < \theta$. Thus, as the contact line advances from the corner onto the ramp, the interface rotates locally by α to form a tight curve, which is subsequently smoothed out over the rest of the interface. Now imagine a stronger contraction with $\alpha > \theta$. If the interface rotates by α at the corner, it would have to penetrate the wall upstream. Hence, a concave corner with a contraction angle larger than the wetting angle appears to present a singularity to the contact line.

This singularity is not real, of course. It arises because the foregoing argument is made in the classical sharp-interface framework, with the interface being viewed as a mathematical surface of zero thickness. This is a good representation of real interfaces as long as the length scale of interest is much larger than the interfacial thickness. At a concave corner of sufficiently large α , the turning of the interface entails intersection with the solid wall, which in

reality would invoke physics on the molecular length scale. Little surprise that an apparent singularity should appear. In fact, a strict implementation of the sharp-interface model would encounter difficulty even for a contact line moving on a *flat* substrate.^{41,42}

This is where the diffuse-interface model presents a distinct advantage. By preserving the reality that interfaces are diffuse mixing layers rather than discontinuities, the model circumvents the traps of singularity on flat substrate as well as at corners. On a flat substrate, Cahn-Hilliard diffusion allows a contact line to move and predicts a dynamic contact angle.^{28,32} Inside a concave corner, diffusion allows the interface to turn a large α in a natural manner as demonstrated in Fig. 5.

We have to point out that the diffuse-interface model introduces a local length scale ϵ , the interfacial thickness. If the physical process being studied involves a length scale that shrinks indefinitely, as occurs here in Fig. 5 and during interfacial pinch-off or rupture,^{43,44} the finite- ϵ effect manifests itself eventually, and is intrinsic to the diffuse-interface formalism. Therefore, the negotiation of the corner in Fig. 5 occurs more slowly with decreasing ϵ . The question of choosing suitable Cahn-Hilliard parameters has been discussed elsewhere.⁴⁵ For the current problem, the diffuse-interface model regularizes the singularity at the corner and captures the qualitative features of the process, but cannot foretell what ϵ value would predict reality quantitatively.

C. Expansion

Wicking through an expansion, schematically depicted in Fig. 6, differs from wicking through a contraction in that the contact line first encounters a convex corner, and then a concave one. The process is illustrated in Fig. 7. When the meniscus is entirely inside the narrower channel upstream, H_w and H_b advance with the same speed. As the contact line reaches the corner at the start of the expansion (point a), it is pinned temporarily according to Gibbs' pinning criterion.⁴⁰ Meanwhile, the base point moves forward very quickly until point b , when the interface reaches an angle of $\theta + \alpha = 85^\circ$ with respect to the upstream wall. It depins from the corner, and the entire meniscus advances through the expansion. This corresponds to the segment between points b and c . At point c , the meniscus reaches the end of the expansion with the contact line at the concave corner. As the wall rotates counterclockwise by α at this corner, so must the interface before it could march downstream onto the straight portion of the tube. This causes a large local curvature of the interface, which propagates toward the center, causing the base point of the meniscus to retreat, as illustrated by the decline of H_b beyond point c . Once this interfacial adjustment is completed at point d , the entire meniscus moves down the wider straight channel, again with the base point and wall point advancing at the same speed.

Naturally one contrasts the above process with wicking through a contraction (Fig. 4). The behavior at the concave corner at the end of the expansion, between points c and d in Fig. 7, is essentially the same as appears at the start of the contraction, from a to b in Fig. 4. If the expansion is too

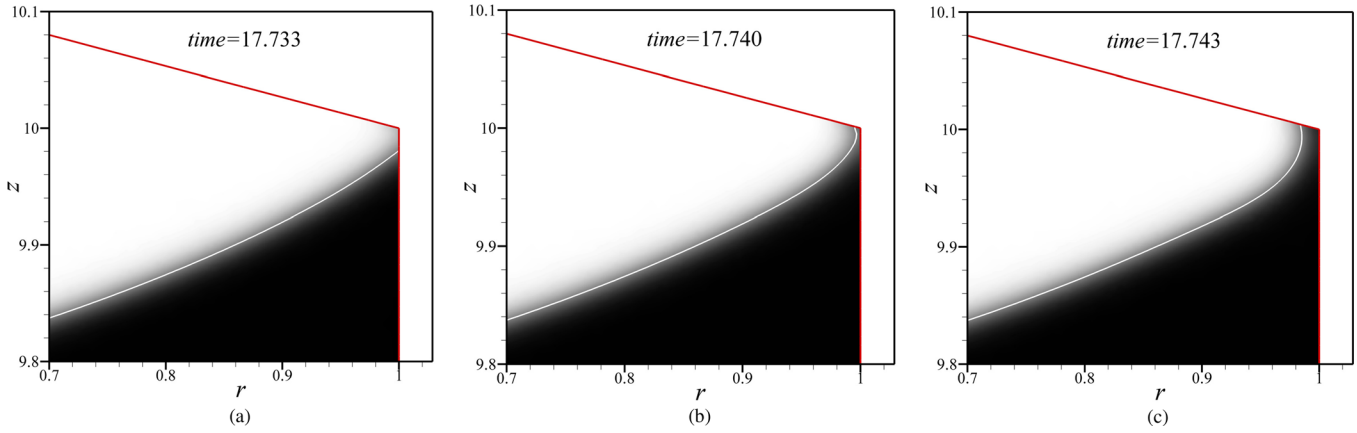


FIG. 5. (Color online) Gray-scale contours of ϕ depicting the interface traversing a concave corner through Cahn-Hilliard diffusion. The light line indicates the contour of $\phi=0$. The contraction angle $\alpha=75^\circ$ is greater than the wetting angle $\theta=60^\circ$. $H_u=10$ and initially the meniscus is at $H_0=9.8$.

abrupt, with $\alpha > \theta$, the corner would present a singularity to a sharp-interface model but not to our Cahn-Hilliard model. On the other hand, the convex corner at the start of the expansion, point *a* in Fig. 7, differs fundamentally from its counterpart, point *c* in Fig. 4; here it has the potential of *permanently* pinning the interface. This would happen if the expansion is abrupt enough such that the required breakthrough angle $\theta_b = \theta + \alpha$ is beyond the maximum achievable $\theta_m = 90^\circ$

$$\alpha + \theta \geq 90^\circ. \tag{14}$$

Such a situation is illustrated by the snapshots in Fig. 8 for $\theta=60^\circ$ and $\alpha=30^\circ$. After the contact line gets pinned at $t=6.6$, the interfacial tension acts to move the rest of the interface forward so as to minimize the interfacial area. This continues till $t=101.6$, when the meniscus becomes a flat surface and can move no further. At this point, the angle between the interface and the upstream wall is $\theta_m=90^\circ$, barely equal to the breakthrough angle θ_b . The contact line cannot depin and the flow is arrested permanently. Thus, the geometric constraint of Eq. (14), based on the Gibbs pinning

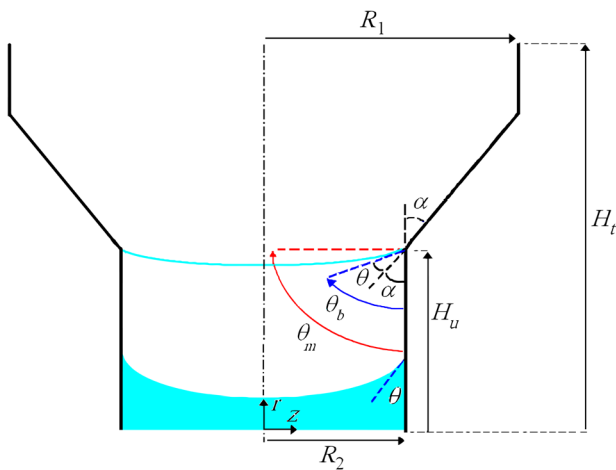


FIG. 6. (Color online) Schematic of an expansion illustrating the pinning criterion. $\theta_b = \alpha + \theta$ is the breakthrough angle, and $\theta_m = 90^\circ$ is the maximum angle that the interface may reach at the corner.

condition,⁴⁰ specifies a degree of expansion beyond which a hydrophilic fluid cannot enter. This may be contrasted with the convex corner at the end of the contraction (point *d* of Fig. 4). As long as the fluid is hydrophilic ($\theta < 90^\circ$), the contact line always depins before the meniscus becomes flat at 90° angle with the downstream wall.

D. Penetration time

The speed of wicking and the time required to penetrate a given depth are of practical significance in various applications^{3,4,16} and have been studied by a few groups.^{15,19} In this subsection, we will examine how the speed of wicking through contractions and expansions is affected by the flow geometry. Consider a tube of total length H_t . The two radii R_1 and R_2 are prescribed, as is the upstream length H_u . The rest of the length consists of a contraction or expansion and possibly a straight downstream segment. The question is what contraction or expansion angle gives the fastest wicking through the total length. We have tested a range of

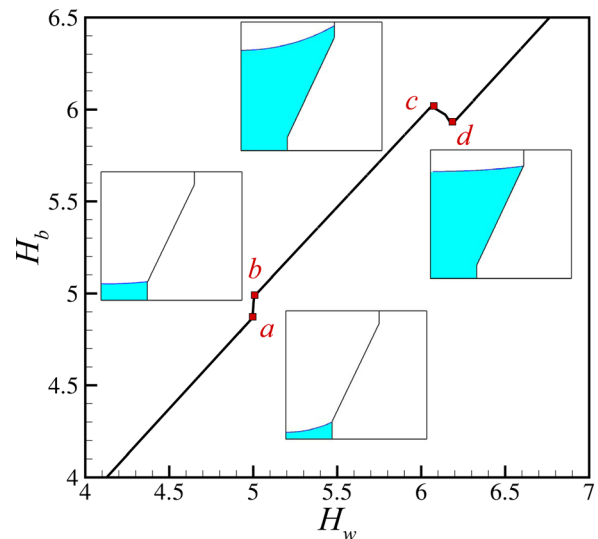


FIG. 7. (Color online) Wicking through an expansion with $\alpha=25^\circ$, $\theta=60^\circ$, $Cn=0.005$, and $H_u=5$. The insets correspond to the four points *a*–*d* on the curve.

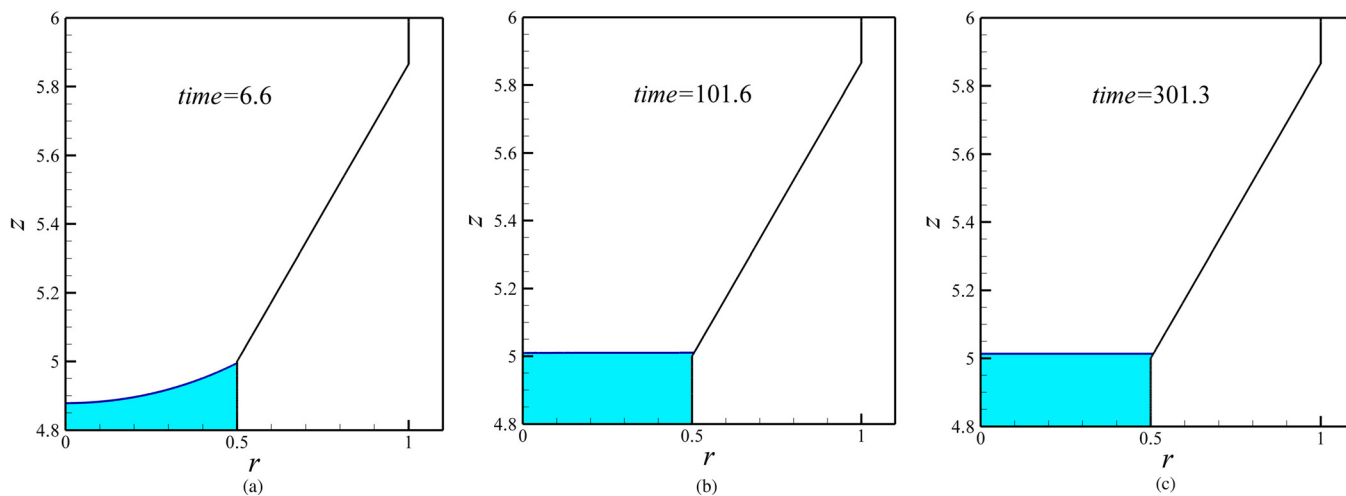


FIG. 8. (Color online) Permanent pinning of the interface at the entrance to an expansion with $\alpha = 30^\circ$, $\theta = 60^\circ$, $C_n = 0.005$, $H_u = 5$, and $H_0 = 4.9$.

contraction/expansion angles and wetting angles. A clear trend emerges and is illustrated in Fig. 9 by comparing $\alpha = 15^\circ$ and 25° for $\theta = 60^\circ$.

In Fig. 9(a), the two trajectories coincide prior to reaching the start of the contraction, point *a*. Afterwards the wicking accelerates faster through the sharper contraction at $\alpha = 25^\circ$, evidently because of the faster increase in curvature and capillary pressure. But the sharper contraction is shorter, and the acceleration ends at point *b*, after which the meniscus enters the narrow downstream segment and decelerates. In comparison, the milder contraction sees a more gradual acceleration that lasts longer, till point *c*. Downstream of point *c*, wicking decelerates as well, but at a gentler rate than in the sharper contraction. This is because the sharper contraction incurs more viscous friction. As a result, the meniscus eventually overtakes that in the sharper contraction, at $H_w \approx 14.8$. Therefore, the question of which geometry gives faster wicking depends on the length of the downstream segment. If it is long enough, a gentler contraction wins. If H_t and H_u are prescribed, then there is an optimal α that gives the shortest penetration time through the entire length. For example, for $H_t = 13$, $H_u = 10$, and $\theta = 60^\circ$, we have tested α

values from 15° to 65° , and $\alpha = 25^\circ$ gives the shortest transit time.

For expansion, the story is simpler (Fig. 9(b)). Wicking is slower in the sharper expansion because the driving force, the capillary pressure, decreases more steeply with the expanding tube radius. This effect is so strong that the sharper expansion (from *a* to *b*) takes longer time to traverse than its milder counterpart (from *a* to *c*) despite its shorter length. Note the sudden surge of H_w at *b* and *c* when the contact line rapidly traverses the concave corner. Upon entering the downstream segment, wicking accelerates to more or less the same speed in both geometries. This speed will gradually decline in the downstream tube. Overall, the sharper expansion always causes a longer penetration time. Besides, comparing Figs. 9(a) and 9(b), the expansion takes much longer time than the contraction of the same length and same α , by 15-fold for $\alpha = 15^\circ$, and 53-fold for 25° . This implies that in a contraction-expansion combination, the latter takes up most of the penetration times.

The penetration or passage time t_p , as it turns out, sheds unique light on the validity of the quasi-static assumption widely used in the literature. By using the formula of Liou

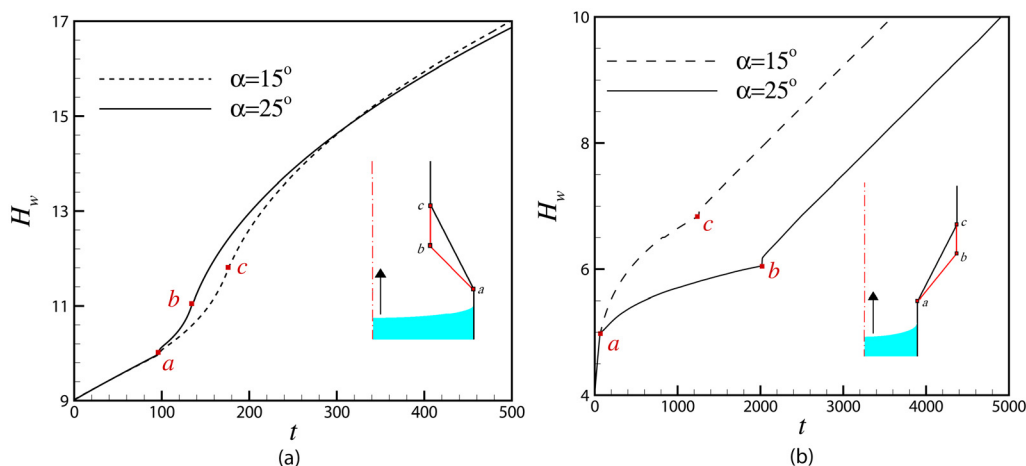


FIG. 9. (Color online) (a) Comparison of wicking speed through 2:1 contractions at two contraction angles $\alpha = 15^\circ$ and 25° . The inset illustrates the flow geometry. $H_u = 10$, $H_0 = 9$, and $\theta = 60^\circ$. (b) Similar comparison for 1:2 expansions at $\alpha = 15^\circ$ and 25° . $H_u = 5$, $H_0 = 4$, and $\theta = 60^\circ$.

et al.,¹⁸ based on a quasi-static spherical interface, we have calculated t_p through expansions at different angles. The formula overpredicts t_p by 2.5% for $\alpha = 5^\circ$, and by 0.81% for $\alpha = 25^\circ$. With increasing α , wicking becomes slower, giving the interface more time to relax toward equilibrium. A different picture emerges for contractions. As α increases from 5° to 25° , the underestimation of t_p by the quasi-static method increases from 16% to 32%. Evidently, a faster moving interface deviates more from the spherical shape and renders the quasi-static assumption less accurate. At large contraction angles, however, another factor comes into play. The strong radial flow tends to restore the meniscus toward spherical (cf. Fig. 4(b)).

To better reflect the flow geometry in porous media, Erickson *et al.*¹⁹ studied wicking through multiple contraction-expansion cycles. They came to the surprising conclusion that as long as the total lengths of the wide segments and narrow segments are each kept constant, the penetration time t_p remains the same regardless of the number of contraction-expansion cycles. This implies that adding additional contraction and expansion pairs costs no delay in the wicking, something inconsistent with our observations in Fig. 9. To probe this further, we compare wicking through three channels with $N = 1, 2,$ and 3 contraction-expansion cycles (Fig. 10). The total lengths of the straight segments are the same among the three, 16 for the wider part and 3 for the narrower part. The sloping segments also add to the same length of 2, and the contraction/expansion angle then increases with N . This geometric setup is modeled after Erickson *et al.*¹⁹

According to Fig. 10, the total penetration time t_p is not the same among the three; it increases by 17% from $N = 1$ to 2 and by another 70% to $N = 3$. As expected, additional contraction-expansion pairs do cost penetration time, more so for larger N as α increases. The discrepancy is mainly because Erickson *et al.*¹⁹ used a much smaller α ($\sim 0.5^\circ$)

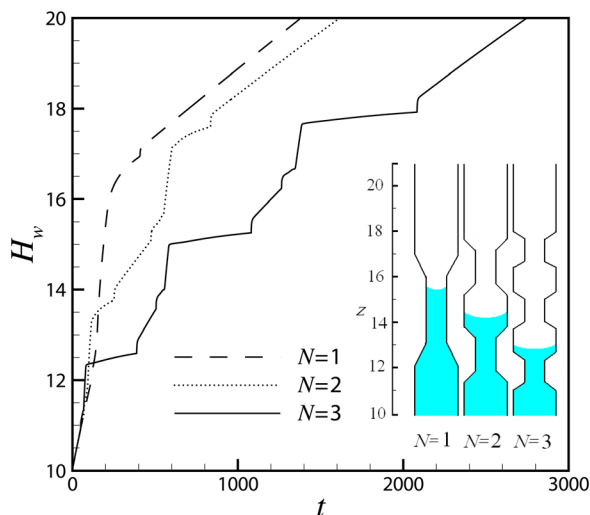


FIG. 10. (Color online) Wicking through multiple contraction-expansion cycles. For $N = 1, 2,$ and 3 , $\alpha = 26.6^\circ, 45^\circ,$ and 56.3° . The wetting angle $\theta = 30^\circ$, $Cn = 0.02$. The total length $H_t = 21$, and the meniscus starts at $H_0 = 10$ at the beginning.

and straight sections much longer than the contractions and expansions. Thus, traversing the contraction and expansion takes up only a small fraction of the total t_p . Moreover, they ignored the local fluid dynamics at the meniscus and replaced it by a quasi-static spherical surface. To probe smaller α in our model, we have computed gentler slopes with α increasing from 1° at $N = 1$ to 15.6° at $N = 16$, with $\theta = 30^\circ$, $R_2/R_1 = 0.75$, $H_u = 10$, and $H_t = 41$. Compared with $N = 1$, t_p increases by a mere 2.1% for $N = 8$ and 11% for $N = 16$. Since Erickson *et al.*¹⁹ only investigated N up to 3, they would not have noticed much change in t_p even if they had not used the quasi-static assumption.

V. WICKING IN Y-SHAPED BRANCHES: CAPILLARY COMPETITION

Connectivity between pores is an important attribute of porous media that has not been considered in the above. When the meniscus reaches the bifurcation where one pore branches into two, will it split into two and go through both branches, or will one branch dominate the other? What parameters determine the interfacial dynamics at and after the bifurcation? These are the questions that we turn to in this section.

Consider the wicking flow in the 2D planar geometry of Fig. 11. The same ambient pressure p_a exists at the far-upstream of the root channel and the far downstream of both branches. When the interface reaches the branching point, it breaks up into two smaller menisci (Fig. 11(b)), each then quickly adjusting to the size of the branches. A bifurcation into two identical branches is a trivial case; wicking proceeds in each branch with equal velocity. If the two branches differ in size, then there is a potential for *capillary competition* governed by the following three factors. (1) The pressure behind each meniscus depends on its curvature and hence the size of the branch. Although the interface is generally non-spherical, we can roughly speak of the capillary pressure in the wide branch p_w being higher than that in the narrow one p_n : $p_w > p_n$. The narrow channel engenders a lower capillary pressure and is thus more conducive to wicking flow. (2) At the junction, we can roughly think of a pressure p_j that is shared by both branches. The pressure drops $p_j - p_w$ and $p_j - p_n$ drive the flow in each branch (Fig. 11(c)). (3) p_j is determined by the viscous friction in the root tube, and continuously rises in time. This is because as wicking proceeds, the flow in one or both branches slows down and so does the flow in the root tube.

Depending on whether p_j is greater than p_w and p_n , we can differentiate two situations: wicking in both branches and wicking in one branch only. The former happens if p_w and p_n differ little, or if the pressure drop expended in the root tube is small such that p_j is initially high. The latter happens if the two branches are disparate in size, or if there is a long and thin root tube to yield a weak p_j . In discussing these two regimes in Subsections V A and V B, we have found it convenient to fix $D_2 = 0.5D_1$ and $L_0 = 4D_1$ and vary the width of the root tube D_0 relative to D_1 . In addition, the contact angle is set at $\theta = 60^\circ$. Length will be scaled by D_1 and time by $\mu_1 D_1 / \sigma$.

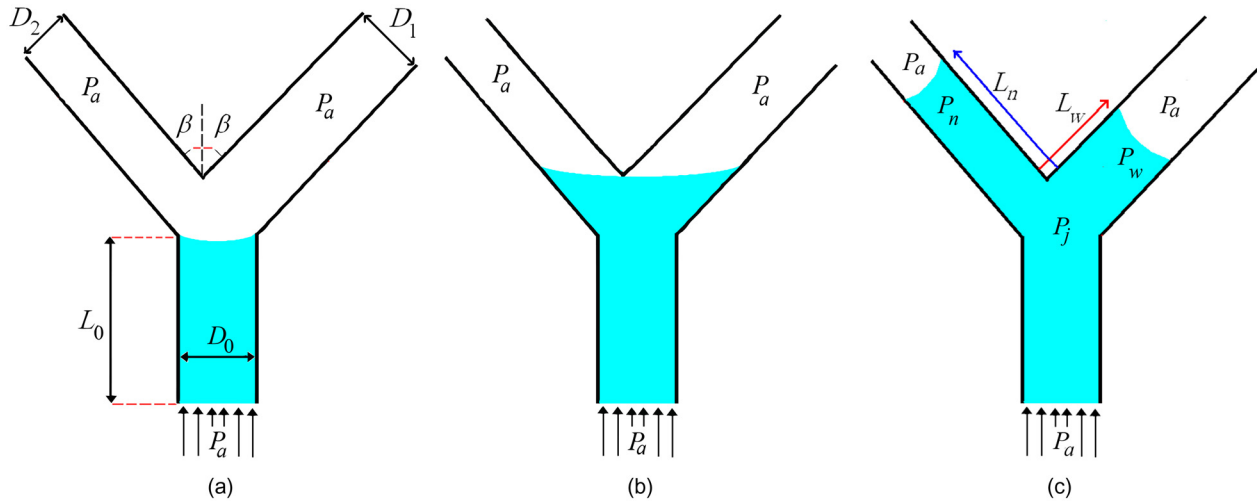


FIG. 11. (Color online) Schematic of a planar microchannel with a Y-shaped bifurcation, showing three stages of wicking: (a) the meniscus reaches the expansion; (b) the meniscus breaks into two at the bifurcation; (c) wicking continues in each branch under suitable conditions.

A. Flow in both branches

With a wide root tube, the viscous dissipation in it is small, and it is like connecting the branches directly to a reservoir. In this simple situation, wicking occurs through both branches, though at different speeds depending on their size (Fig. 12).

When the meniscus reaches the end of the root tube (Fig. 11(a)), it faces an expansion at angle β , and the discussion of pinning in Subsection IV C applies. In particular, we require $\beta < 90^\circ - \theta$ such that the meniscus can depin from the corner and proceed beyond this point. Throughout this section, we have used $\beta = 20^\circ$. When the interface reaches the point of bifurcation (Fig. 11(b)), it breaks into two smaller menisci, whose curvature, at this point, reflects the larger dimension of the junction. Thus, they are not at equilibrium with the smaller size of each branch. A short period

of equilibration ensues, with the wall points on the outside walls pulling back and those on the walls in the middle surging ahead. This is why in Fig. 12, the curves appear to start from a small positive L value at $t = 0$. In the inset, points a and b mark when the equilibration is completed in the narrow and wide branches, respectively. Note that the bifurcation angle β determines the size of the meniscus in Fig. 11(b) and the equilibration process. But it has a little effect on the subsequent wicking in each branch. Once the equilibration is completed, each meniscus is orientated symmetrically with respect to the axis of its branch. The geometric setup is such that the pressure p_j is higher than both p_n and p_w , and wicking proceeds in both branches.

Initially, the narrow tube enjoys faster wicking, because the pressure drops $p_j - p_n$ driving the flow is larger than its counterpart in the wide tube. This lasts till $t \approx 11$, marked by point c in the inset of Fig. 12. As the liquid continues to invade both branches, the viscous dissipation increases with the column height, and the flow speed declines. This effect is stronger for the narrow branch since, as the flow approaches the Poiseuille flow, the viscous wall stress scales with the meniscus velocity divided by the channel width. Thus, the wider tube has faster wicking for later times, similar to the prediction of the Lucas-Washburn equation.

Once the flow starts in either branch, it does not stop in finite time. This is because p_j must exceed the pressure p_n or p_w for there to be flow in the branch. In time p_j and hence the pressure drop only increases as the flow, and pressure drop in the root tube declines. Thus, the flow continues in both branches, and gradually slows down toward zero in time.

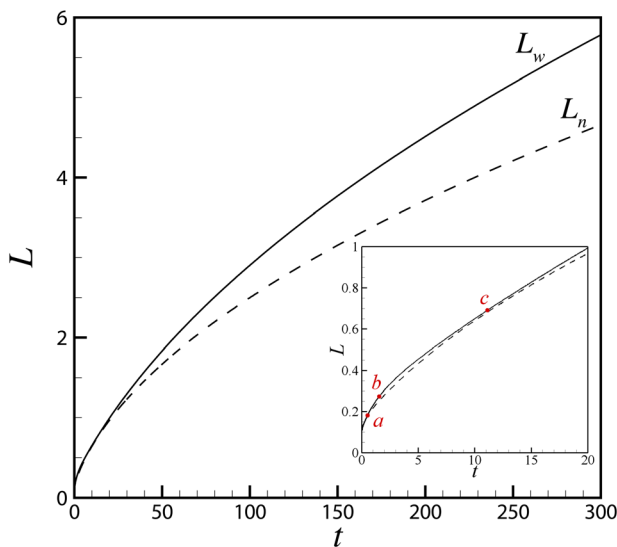


FIG. 12. (Color online) Wicking in both branches with a relatively wide root tube: $D_0 = 1.6$. The origin of time is when the meniscus first touches the tip at the junction (cf. Fig. 11(b)). The inset shows that wicking is faster in the narrow branch initially ($t < 11$), but the wide branch wins for longer times.

B. Flow in one branch

With thinner root tubes, p_j may initially fall below the capillary pressure p_w in the wide branch such that wicking occurs only in the narrow branch. This behavior is demonstrated for $D_0 = 0.6$ by the trajectories of the menisci in Fig. 13 and by the snapshots of the interface in Fig. 14. After the interface splits into two at the bifurcation, they reorient with respect to the axes of the branches and adjust their

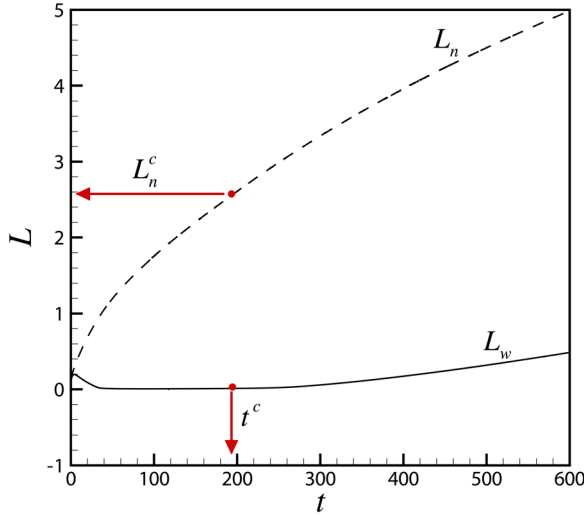


FIG. 13. (Color online) Capillary competition between two branches with a relatively narrow root tube, $D_0=0.6$. Wicking proceeds in the narrow branch but is suppressed in the wide branch until $t^c=194$, marked by a dot on both curves. The origin of time is when the meniscus first touches the tip at the junction (cf. Fig. 11(b)).

curvature to the local tube size (Fig. 14(b)). Afterwards wicking starts in the narrow branch, and the flow in the root tube entails a pressure drop. The junction pressure p_j thus produced turns out to be lower than the capillary pressure p_w in the wide branch, and no wicking occurs there. In fact, the negative pressure $p_j - p_w$ causes the interface to *retreat* until the contact line becomes pinned at the inner corner at $t=42$. Figure 14(c) depicts a moment soon afterwards with the meniscus immobilized in the wide branch. But the arrest of flow in the wide branch is necessarily temporary. As the flow slows down in the narrow tube, p_j rises continually, eventually surpassing p_w to produce wicking flow in the wide branch as well. This is marked in Fig. 13 by $t^c=194$ when the liquid column in the narrow tube is at $L_n^c=2.56$. After that the situation becomes qualitatively the same as in Fig. 12, and Fig. 14(d) shows a snapshot in this stage. Eventually wicking slows down toward zero in both branches.

The onset of wicking in the wide branch, indicated by t^c or L_n^c , is of practical interest. For instance, in a porous medium of finite thickness, the critical value L_n^c for the small pores will determine whether the bigger pores will contribute to liquid transport at all. If the liquid traverses the entire length of the smaller pores before wicking even starts in the bigger ones, the latter will be dead ends, which have been observed in experiments⁴⁶ and considered a major hindrance to water transport through the GDM of fuel cells.²⁰ Note that all the ideas and qualitative arguments discussed so far in this section apply as well to 3D flows in real porous media.

In the spirit of the Lucas-Washburn analysis (Eq. (13)), we can estimate the onset of wicking in the wide branch by neglecting dynamics at the menisci and assuming fully developed Poiseuille flow in the root and narrow tubes. Let us denote the instantaneous average velocity in the narrow tube by V_2 and that in the root tube by V_0 . Then, the junction

pressure p_j can be estimated either from the force balance on the liquid in the root tube or that in the narrow tube

$$p_j = p_a - \frac{12\mu L_0 V_0}{D_0^2} = p_a - \frac{2\sigma \cos \theta}{D_2} - \frac{12\mu L_n V_2}{D_2^2}. \quad (15)$$

The critical condition for wicking in the wide tube is p_j being equal to the capillary pressure behind the meniscus in the wide tube

$$p_j = p_w = p_a - \frac{2\sigma \cos \theta}{D_1}. \quad (16)$$

In addition, volume conservation requires $V_0 D_0 = V_2 D_2$. Eliminating V_0 and V_2 from the above gives the following critical condition on the liquid column L_n^c :

$$L_n^c = L_0 \left(\frac{D_1}{D_2} - 1 \right) \left(\frac{D_2}{D_0} \right)^3. \quad (17)$$

Recall our previous argument that wicking in the wide tube depends on the viscous friction in the root tube and the dissimilarity between the two branches. It is no surprise that L_n^c turns out to depend on the length and diameter of the root tube as well as the size difference between the two branches. For the conditions in Fig. 13, Eq. (17) predicts $L_n^c=2.3$, reasonably close to the numerical result of 2.56. Numerical experimentation with narrower D_0 values has confirmed further delays in the wide branch in agreement with Eq. (17). Finally, we note that the above calculation can be easily generalized to 3D circular tubes, and the formula has the exponent on (D_2/D_0) changed from 3 to 4.

C. Flow reversal due to spatially inhomogeneous hydrophilicity

Insofar as the Young-Laplace equation gives a capillary pressure in the form of $\sigma \cos \theta / D$, varying the contact angle θ in a branch is in a way tantamount to varying the tube size D . Thus, capillary competition between branches can be controlled by varying θ as well as D . Suppose that in Fig. 11, we make the downstream portion of the wide branch more hydrophilic, with a smaller contact angle. Then, a *flow reversal* may occur in the narrow channel, as illustrated in Fig. 15.

In this geometry, $\theta=60^\circ$ throughout the Y-branch except for the downstream portion of the wide branch starting from $L_w=1.25$ that features a smaller $\theta=20^\circ$. The geometric and physical parameters of the setup are such that wicking occurs initially only in the narrow branch and starts later in the wide channel around $t=110$. When the meniscus encounters the more hydrophilic portion in the wide branch ($t=942$), the wicking suddenly accelerates, causing a flow reversal in the narrow tube. This is because the elevated flow rate in the root tube depresses the pressure at the junction so much that it falls below the capillary suction pressure p_n in the narrow tube.

Depending on the physical and geometric parameters, the liquid column may retreat entirely from the narrow tube, with the interface pinned at the corner of the bifurcation, or reverse its course again before that. Thereafter, the situation

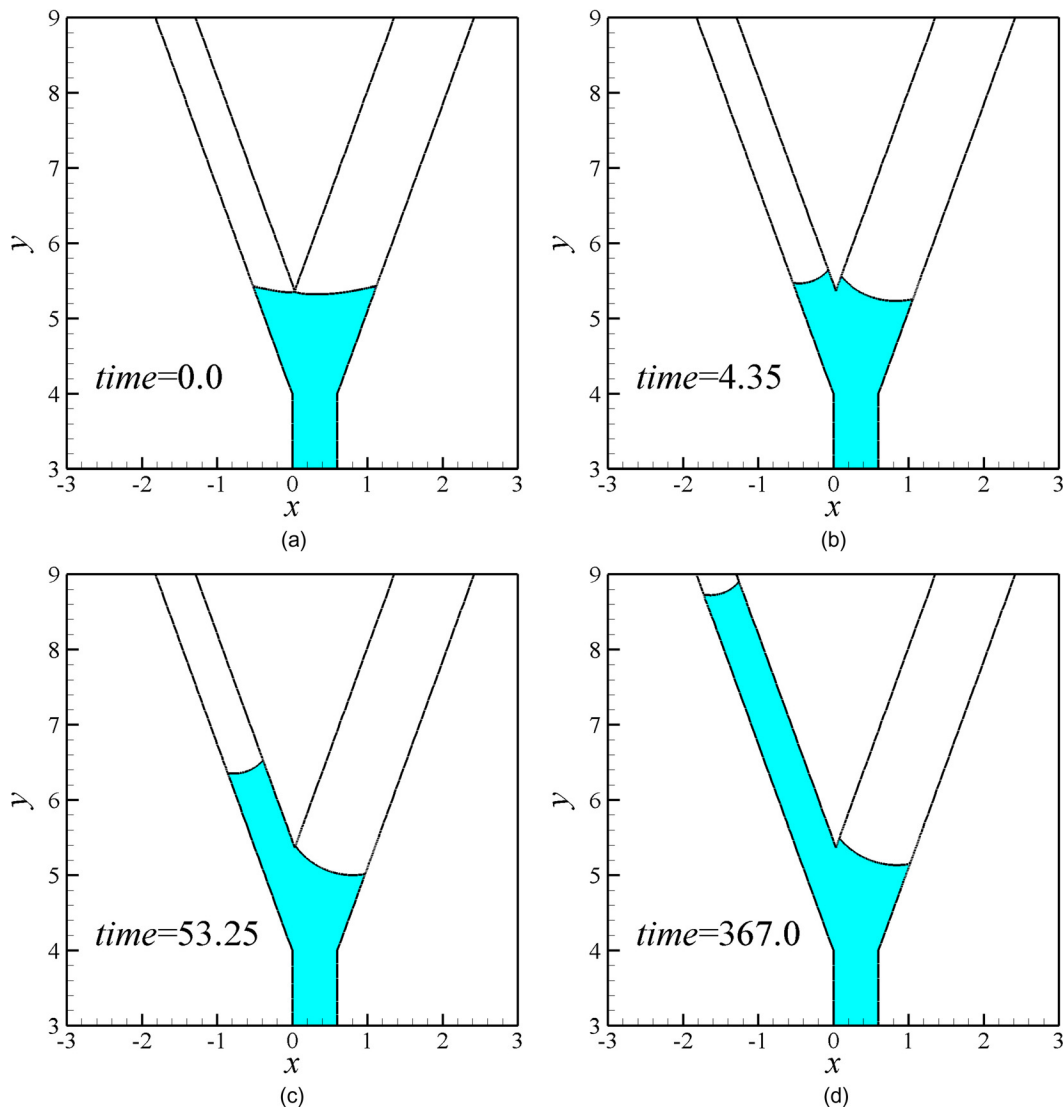


FIG. 14. (Color online) Evolution of the interfacial morphology for the simulation depicted in Fig. 13. (a) The meniscus touches the salient corner at $t=0$. (b) The meniscus relaxes toward the equilibrium curvature inside each branch. (c) After a brief retraction, the meniscus is immobilized in the wide branch. (d) After the restarting of flow in the wide branch, the menisci advance in both branches.

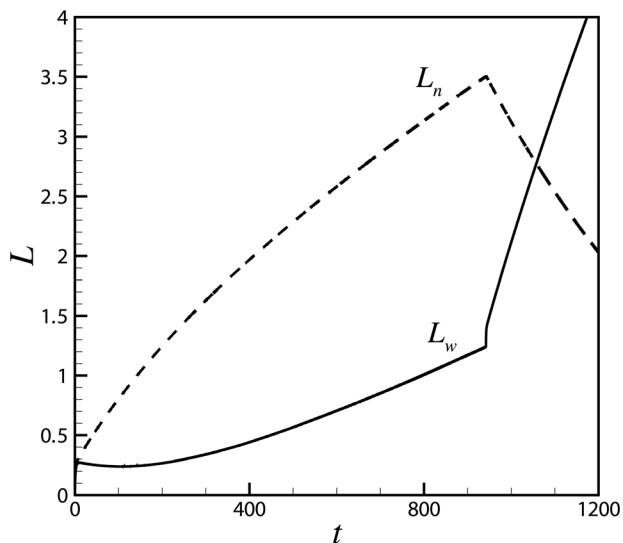


FIG. 15. Flow reversal in the narrow branch when the meniscus in the wide branch moves onto a more hydrophilic portion with $\theta=20^\circ$ at $L_w=1.25$. Elsewhere $\theta=60^\circ$. $D_0=0.6$, $L_0=4$, and $D_2=0.9$.

becomes similar to Fig. 13 or 12. Based on the Young-Laplace equation, one may view the wicking in the more hydrophilic portion of the wide branch as occurring in a tube with $\theta=60^\circ$ but a *smaller effective width* $D_e=D_1\cos 60^\circ/\cos 20^\circ=0.53D_1$, which is narrower than D_2 . (The viscous friction will be different, of course.) Thus, the wicking continues with dwindling speed in the wide branch until the junction pressure has again risen above the capillary pressure in the narrow tube to restart wicking there.

Such flow reversal has been observed experimentally. Litster *et al.*²⁰ reported that in a model GDM for fuel cells, a sudden acceleration in one flow path, due to breakthrough from the GDM into open space, causes the liquid to retreat in a neighboring connected path. The underlying principle is simple and robust and suggests how surface properties can be manipulated to control the flow pattern in porous media. Indeed, the GDM of fuel cells is often surface-treated in a spatially inhomogeneous way to enhance water transport.⁴⁷ In addition, a more hydrophilic micro-porous layer with finer pores is often attached to the GDM to create a jump in

wettability along the flow direction.⁴⁸ Another potential application for capillary competition and flow reversal is as a precise switching mechanism in microfluidic devices.^{49–51} By careful choice of the root and branch sizes, it is possible to design a flow loop in which different branches are impregnated by liquid at precise moments. The mechanism of capillary competition works for multiple branches as well, and one may design microfluidic manifolds using the same principle.

VI. CONCLUDING REMARKS

This work aims for a detailed and rational understanding of two-phase transport through micropores in porous media. Using finite-element computations, we capture the evolving morphology of the interfaces in geometries that retain the salient features of real pores, including expansion, contraction, and branching. From a fundamental viewpoint, the most important findings are the following:

- (a) The meniscus undergoes complex deformation during transit through micropores, governed by the dynamic balance among fluid-solid and gas-liquid interfacial tensions and viscous friction. Such flow effects tend to distort the meniscus away from a spherical shape.
- (b) The dynamics of the contact line plays a central role. It pins at protruding corners, potentially barring wicking into expansions with too steep a slope. The contact line negotiates inner corners, thanks to the diffuseness of the interface.
- (c) Capillary competition between connected branches depends on the capillary pressure due to meniscus curvature inside each, and in turn on the size of the branches and surface wettability. Under suitable conditions, wicking can be arrested in wider branches in favor of a narrower one, and the flow may even reverse course when wicking accelerates in a neighboring path.

We have hinted at the relevance of these insights to technological applications, e.g., in proton-membrane exchange fuel cells. Against this background, however, the work reported here must be seen as a preliminary step. Real 3D flow through porous media includes many complicating factors that have not been accounted for, including 3D connectivity, pore size distribution and tortuosity of the flow path. Nevertheless, this serves as a starting point for an approach to two-phase flow in porous media that is more rational and accurate than the traditional one centered on an empirical relative permeability.

ACKNOWLEDGMENTS

This work was supported by an NSERC Strategic Project Grant. We thank G. H. (Bud) Homsy of UBC, Simon Liu of NRC Institute for Fuel Cell Innovation, and John Shen of Palcan Fuel Cell Co. Ltd. for helpful discussions. J.J.F. also acknowledges partial support from the Petroleum Research Fund, the Canada Research Chair program, NSERC (Discovery and Accelerator programs), and the Canada Foundation for Innovation.

- ¹H. Czachor, "Modeling the effect of pore structure and wetting angles on capillary rise in soils having different wettabilities," *J. Hydrol.* **328**, 604 (2006).
- ²E. C. Kumbur and K. V. Sharp, "On the effectiveness of Leverett approach for describing the water transport in fuel cell diffusion media," *J. Power Sources* **168**, 356 (2007).
- ³J. H. Nam and M. Kaviani, "Effective diffusivity and water-saturation distribution in single- and two-layer PEMFC diffusion medium," *Int. J. Heat Mass Transfer* **46**, 4595 (2003).
- ⁴S. Bouaidat, O. Hansen, H. Bruus, C. Berendsen, N. K. Bau-Madsen, P. Thomsen, A. Wolff, and J. Jonsmann, "Surface-directed capillary system; theory, experiments and applications," *Lab Chip* **5**, 827 (2005).
- ⁵J. M. Chen, P. C. Huang, and M. G. Lin, "Analysis and experiment of capillary valves for microfluidics on a rotating disk," *Microfluid. Nanofluid.* **4**, 427 (2008).
- ⁶R. Lucas, "Ueber das zeitgesetz des kapillaren aufstiegs von flüssigkeiten," *Kolloid-Z.* **23**, 15 (1918).
- ⁷E. W. Washburn, "The dynamics of capillary flow," *Phys. Rev.* **17**, 273 (1921).
- ⁸C. H. Bosanquet, "On the flow of liquids into capillary tubes," *Philos. Mag. Ser. 6* **45**, 525 (1923).
- ⁹R. Siegel, "Transient capillary rise in reduced and zero-gravity fields," *J. Appl. Mech.* **83**, 165 (1961).
- ¹⁰P. Joos, P. Van Remoortere, and M. Bracke, "The kinetics of wetting in a capillary," *J. Colloid Interface Sci.* **136**, 189 (1990).
- ¹¹M. Dreyer, A. Delgado, and H. J. Rath, "Capillary rise of liquid between parallel plates under microgravity," *J. Colloid Interface Sci.* **163**, 158 (1994).
- ¹²B. V. Zhmud, F. Tiberg, and K. Hallsténsson, "Dynamics of capillary rise," *J. Colloid Interface Sci.* **228**, 263 (2000).
- ¹³G. J. Gutierrez, A. Medina, and F. J. Higuera, "Equilibrium height of a liquid in a gap between corrugated walls under spontaneous capillary penetration," *J. Colloid Interface Sci.* **338**, 519 (2009).
- ¹⁴R. Sharma and D. S. Ross, "Kinetics of liquid penetration into periodically constricted capillaries," *J. Chem. Soc., Faraday Trans.* **87**, 619 (1991).
- ¹⁵T. L. Staples and D. G. Shaffer, "Wicking flow in irregular capillaries," *Colloids Surf., A* **204**, 339 (2002).
- ¹⁶D. Patro, S. Bhattacharyya, and V. Jayaram, "Flow kinetics in porous ceramics: Understanding with non-uniform capillary models," *J. Am. Ceram. Soc.* **90**, 3040 (2007).
- ¹⁷M. Reyssat, L. Courbin, E. Reyssat, and H. A. Stone, "Imbibition in geometries with axial variations," *J. Fluid Mech.* **615**, 335 (2008).
- ¹⁸W. W. Liou, Y. Peng, and P. E. Parker, "Analytical modeling of capillary flow in tubes of nonuniform cross section," *J. Colloid Interface Sci.* **333**, 389 (2009).
- ¹⁹D. Erickson, D. Li, and C. B. Park, "Numerical simulation of the capillary driven flows in non-uniform cross sectional capillaries," *J. Colloid Interface Sci.* **250**, 422 (2002).
- ²⁰S. Litster, D. Sinton, and N. Djilali, "Ex situ visualization of liquid water transport in PEM fuel cell gas diffusion layers," *J. Power Sources* **154**, 95 (2006).
- ²¹N. Djilali, "Computational modelling of polymer electrolyte membrane (PEM) fuel cells: Challenges and opportunities," *Energy* **32**, 269 (2007).
- ²²U. Pasaogullari and C. Y. Wang, "Liquid water transport in gas diffusion layer of polymer electrolyte fuel cells," *J. Electrochem. Soc.* **151**, A399 (2004).
- ²³G.-G. Park, Y.-J. Sohn, T.-H. Yang, Y.-G. Yoon, W.-Y. Lee, and C.-S. Kim, "Effect of PTFE contents in the gas diffusion media on the performance of PEMFC," *J. Power Sources* **131**, 182 (2004).
- ²⁴D. Jacqmin, "Contact-line dynamics of a diffuse fluid interface," *J. Fluid Mech.* **402**, 57 (2000).
- ²⁵J. W. Cahn and J. E. Hilliard, "Free energy of a non-uniform system. Part I: interfacial free energy," *J. Chem. Phys.* **28**, 258 (1958).
- ²⁶D. Jacqmin, "Calculation of two-phase Navier-Stokes flows using phase-field modeling," *J. Comput. Phys.* **155**, 96 (1999).
- ²⁷P. Yue, C. Zhou, J. J. Feng, C. F. Ollivier-Gooch, and H. H. Hu, "Phase-field simulations of interfacial dynamics in viscoelastic fluids using finite elements with adaptive meshing," *J. Comput. Phys.* **219**, 47 (2006).
- ²⁸P. Yue and J. J. Feng, "Wall energy relaxation in the Cahn-Hilliard model for moving contact lines," *Phys. Fluids* **23**, 012106 (2011).
- ²⁹C. Zhou, P. Yue, J. J. Feng, C. F. Ollivier-Gooch, and H. H. Hu, "3D phase-field simulations of interfacial dynamics in Newtonian and viscoelastic fluids," *J. Comput. Phys.* **229**, 498 (2010).

- ³⁰D. Zhou, P. Yue, and J. J. Feng, "Viscoelastic effects on drop deformation in a converging pipe flow," *J. Rheol.* **52**, 469 (2008).
- ³¹P. Gao and J. J. Feng, "Enhanced slip on a patterned substrate due to depinning of contact line," *Phys. Fluids* **21**, 102102 (2009).
- ³²P. Yue, C. Zhou, and J. J. Feng, "Sharp-interface limit of Cahn-Hilliard model for moving contact lines," *J. Fluid Mech.* **645**, 279 (2010).
- ³³P. Gao and J. J. Feng, "A numerical investigation of the propulsion of water walkers," *J. Fluid Mech.* **668**, 363 (2011).
- ³⁴M. Ahmadvouydarab, Z. S. Liu, and J. J. Feng, "Interfacial flows in corrugated microchannels: Flow regimes, transitions and hysteresis," *Int. J. Multiphase Flow* **37**, 1266 (2011).
- ³⁵L. A. Freitag and C. Ollivier-Gooch, "Tetrahedral mesh improvement using swapping and smoothing," *Int. J. Numer. Methods Eng.* **40**, 3979 (1997).
- ³⁶G. Caginalp and X. Chen, "Convergence of the phase field model to its sharp interface limits," *Eur. J. Appl. Math.* **9**, 417 (1998).
- ³⁷P. Yue, J. J. Feng, C. Liu, and J. Shen, "A diffuse-interface method for simulating two-phase flows of complex fluids," *J. Fluid Mech.* **515**, 293 (2004).
- ³⁸P. Yue, C. Zhou, and J. J. Feng, "Spontaneous shrinkage of drops and mass conservation in phase-field simulations," *J. Comput. Phys.* **223**, 1 (2007).
- ³⁹R. G. Cox, "The dynamics of the spreading of liquids on a solid surface. Part I: Viscous flow," *J. Fluid Mech.* **168**, 169 (1986).
- ⁴⁰S. Herminghaus, M. Brinkmann, and R. Seemann, "Wetting and dewetting of complex surface geometries," *Annu. Rev. Mater. Res.* **38**, 101 (2008).
- ⁴¹L. M. Pismen, "Nonlocal diffuse interface theory of thin films and the moving contact line," *Phys. Rev. E* **64**, 021603 (2001).
- ⁴²L. M. Pismen, "Mesoscopic hydrodynamics of contact line motion," *Colloids Surf., A* **206**, 11 (2002).
- ⁴³P. Yue, C. Zhou, and J. J. Feng, "A computational study of the coalescence between a drop and an interface in Newtonian and viscoelastic fluids," *Phys. Fluids* **18**, 102102 (2006).
- ⁴⁴P. Gao and J. J. Feng, "Spreading and breakup of a compound drop on a partially wetting substrate," *J. Fluid Mech.* **682**, 415 (2011).
- ⁴⁵P. Yue and J. J. Feng, "Can diffuse-interface models quantitatively describe moving contact lines?," *Eur. Phys. J. Spec. Top.* **197**, 37 (2011).
- ⁴⁶R. C. Goodknight, W. A. Klikoff, and I. Fatt, "Non-steady-state fluid flow and diffusion in porous media containing dead-end pore volume," *J. Phys. Chem.* **64**, 1162 (1960).
- ⁴⁷G. Lin and T. V. Nguyen, "Effect of thickness and hydrophobic polymer content of the gas diffusion layer on electrode flooding level in a PEMFC," *J. Electrochem. Soc.* **152**, A1942 (2005).
- ⁴⁸T. Tanuma, "Innovative hydrophilic microporous layers for cathode gas diffusion media," *J. Electrochem. Soc.* **157**, B1809 (2010).
- ⁴⁹G. Blankenstein and U. D. Larsen, "Modular concept of a laboratory on a chip for chemical and biochemical analysis," *Biosens. Bioelectron.* **13**, 427 (1998).
- ⁵⁰G.-B. Lee, C.-I. Hung, B.-J. Ke, G.-R. Huang, and B.-H. Hwei, "Micromachined pre-focused $1 \times N$ flow switches for continuous sample injection," *J. Micromech. Microeng.* **11**, 567 (2001).
- ⁵¹R. Chein and S. H. Tsai, "Microfluidic flow switching design using volume of fluid model," *Biomed. Microdevices* **6**, 81 (2004).